THE UNIVERSITY of EDINBURGH

Edinburgh Research Explorer

Structural degradation of sands during cyclic liquefaction: Insight from DEM simulations

Citation for published version:
Huang, X, Hanley, KJ, Zhang, Z & Kwok, FCY 2019, 'Structural degradation of sands during cyclic liquefaction: Insight from DEM simulations', *Computers and Geotechnics*, vol. 114. https://doi.org/10.1016/j.compgeo.2019.103139

Digital Object Identifier (DOI):
10.1016/j.compgeo.2019.103139

Link:
Link to publication record in Edinburgh Research Explorer

Document Version:
Peer reviewed version

Published In:
Computers and Geotechnics

General rights
Copyright for the publications made accessible via the Edinburgh Research Explorer is retained by the author(s) and / or other copyright owners and it is a condition of accessing these publications that users recognise and abide by the legal requirements associated with these rights.

Take down policy
The University of Edinburgh has made every reasonable effort to ensure that Edinburgh Research Explorer content complies with UK legislation. If you believe that the public display of this file breaches copyright please contact openaccess@ed.ac.uk providing details, and we will remove access to the work immediately and investigate your claim.

Download date: 05. May. 2023

Structural degradation of sands during cyclic liquefaction: Insight from DEM simulations

Xin Huang[1,2*], Kevin J. Hanley[3], Zixin Zhang[1,2], Chung-yee Kwok[4]

[1]Department of Geotechnical Engineering, Tongji University

[2]State Key Laboratory of Geotechnical and Underground Engineering, Ministry of Education, Tongji University,1239 Siping Road, Shanghai 200092, China

[3]School of Engineering, Institute for Infrastructure and Environment, The University of Edinburgh, Edinburgh EH9 3JL, UK

[4]Department of Geotechnical Engineering, The University of Hong Kong, Pokfulam Road, Hong Kong, China

*Corresponding author, Email: xhuang@tongji.edu.cn

Declarations of interest: none

Abstract

The macro stress–strain responses of sands are closely related to the evolution of the force transmission network. In this paper, variations of the mechanical stability and reversibility of the force transmission network during the cyclic liquefaction process are explored using discrete element method (DEM) simulations. It is shown that sands degrade gradually from hyperstatic states to isostatic states during cyclic loading and become hypostatic when approaching liquefaction. During this process, the number of excessive contacts decreases gradually and the sample becomes unjammed. An effective and resilient force transmission network should contain enough mechanically stable particles to spread throughout the entire sample. Structural degradation during cyclic loading towards liquefaction is associated with decreasing reversibility of the force transmission network that is characterized by increasing mean squared displacement, increasing fraction of broken contacts and decreasing size of the largest force transmission network. Flow deformation and the development of significant double-amplitude axial strain are attributed to the inability of a large proportion of the broken contacts to re-form post-liquefaction. The size of the largest force transmission network (S_L) decays linearly with mean effective stress and there exists a critical value of S_L below which liquefaction will occur.

Keywords: Cyclic liquefaction; Mechanical stability; Reversibility; DEM

1 Introduction

Flow liquefaction and cyclic mobility are the two liquefaction phenomena typical for saturated sands under undrained cyclic loading conditions [1]. The former is mainly observed for loose sand which suddenly loses its strength and stiffness and flows in an uncontrollable manner upon liquefaction; the latter occurs in medium dense to dense sands, and is characterized by the progressive development of shear deformation in the process of repeating loss and gain of strength and stiffness after initial liquefaction. Both will result in excessive ground deformation and cause damage to infrastructure during earthquakes. Therefore, liquefaction potential and the triggering conditions for these two phenomena have been extensively studied by the geotechnical community through well-controlled laboratory tests [2-7]. Based on the experimental observations, a number of constitutive models have been established to predict the pre- and post-liquefaction behavior of sands [8-12]. Some of these constitutive models incorporated correlations between macro stress–strain behavior and micro-structure evolution. However, since it is difficult to obtain micro-scale information in most laboratory tests, those hypotheses incorporated in constitutive models are mostly phenomenological and need to be verified [13].

Discrete element method (DEM) [14] simulations can provide both macro stress–strain responses and particle-scale information. It is an effective tool for exploring the fundamental mechanisms underlying the macro-scale phenomena. DEM has been shown to be able to capture a variety of soil behavior at both small-strain [15-17] and large-strain levels [18-19]. DEM has also been used to simulate the cyclic liquefaction behavior of sands and evolution laws for some contact-based fabric variables during cyclic loading have been reported [20-24]. Besides traditional contact-based fabric descriptors, some void-based fabric indices were also proposed and found to have good correlations with macro-scale cyclic stress–strain behavior. For example, Wang and Wei [25] used the difference between the particle center and the Voronoi cell center (centroid distance) to describe the micro-structural evolution of sands both pre- and post-liquefaction. Wang et al. [26] evaluated correlations between different parameters and post-liquefaction shear strain and found that the new fabric index they proposed, Mean Neighboring Particle Distance (MNPD), had the best correlation with post-liquefaction shear strain development. Wei et al. [13] proposed two void-based fabric indices to quantify the anisotropy of local void distribution, based on which a

unique hardening line that separates flow and jamming states was identified. It is noted that DEM can only qualitatively represent a soil's behavior unless the real texture and shape of the soil grains are captured which is seldom done (including in this study). Both the texture and shape of soil grains significantly affect the physical as well as the mechanical properties of soils [37]. Nevertheless, the qualitative insights provided by smooth-sphere-based DEM are valuable for understanding the particle-scale mechanisms underlying the macroscopic stress–strain responses.

It is noteworthy that most of the aforementioned studies were focused on the rearrangement and characteristics of particles, contacts or voids. For granular materials, external loads are transferred through clusters of contacting particles, i.e., force chains. Most of the external load applied to a granular system such as soil is borne by 'strong force chains', comprising a subset of the particles in the system [27-28]. The progressive loss of strength and stiffness during cyclic loading as liquefaction is approached should be closely related to the rheology and stability of this major force transmission network. This, however, has not yet been well understood. This study explores the evolution of mechanical stability and reversibility of the force transmission network through DEM simulations. It will be shown that both flow liquefaction and cyclic mobility are related to the progressive degradation of the major force transmission network during cyclic loading, which becomes mechanically unstable upon liquefaction.

2 Overview of DEM Simulations

The simulations were run using the commercial software PFC3D [29]. A cloud of 19449 initially non-contacting spheres were generated at half of their required sizes within a cylindrical domain bounded by rigid walls. The particles were then expanded and equilibrated until their target sizes were reached. The particle size distribution (PSD) follows the grading curve of Toyoura sand (Figure 1). Note that particles smaller than 0.115 *mm* were truncated as these particles make a negligible contribution to the overall volume-based PSD but can significantly increase the simulation time. A simplified Hertz–Mindlin contact model was adopted with a particle shear modulus of 29 *GPa* and a Poisson's ratio of 0.12. Gravitational forces were neglected. Isotropic compression was performed until the mean effective stress (p') of the assembly reached 500 *kPa*. During this procedure, an interparticle friction coefficient of 0.3 was used to generate a looser

sample with a void ratio of 0.692, while a second, denser sample with a void ratio of 0.658 was created using an interparticle friction coefficient of 0.25. It is noteworthy that since only a small range of packing density can be achieved due to the use of spherical particles and it is difficult to calculate the relative density of a DEM sample accurately, whether a sample was in a 'dense' or a 'loose' state was judged from whether it dilated or contracted during triaxial shearing in the current DEM simulations. It has been shown [30] that when rotational resistance is absent, the critical-state angle of shearing resistance of a DEM assembly composed of spheres will be independent of the interparticle friction coefficient when it exceeds 0.5. Therefore, the interparticle friction coefficient was increased to 0.5 and the assemblies were again equilibrated after isotropic compression. The generated samples were then subjected to constant-volume cyclic loading with the deviatoric stress q following a sinusoidal variation with time (t):

$$q = q_{cyc}\sin(\omega t) \qquad \text{(Eq. 1)}$$

in which q_{cyc} is the cyclic stress amplitude and ω is the angular frequency. This kind of loading path has been widely adopted and serves as the standard testing scheme for evaluating the liquefaction potential of sand [2,5,6,31,32]. A parametric study showed that when ω was below 10π rad/s it would not have an obvious influence on the simulation results [24]. Therefore, ω was taken to be 10π rad/s. To ensure the sample flowed or liquefied within a reasonable number of loading cycles (N), q_{cyc} was selected to be 150 *kPa* for the looser sample, which corresponds to a critical stress ratio of 0.3; q_{cyc} was equal to 200 *kPa* for the denser sample, which corresponds to a critical stress ratio of 0.4.

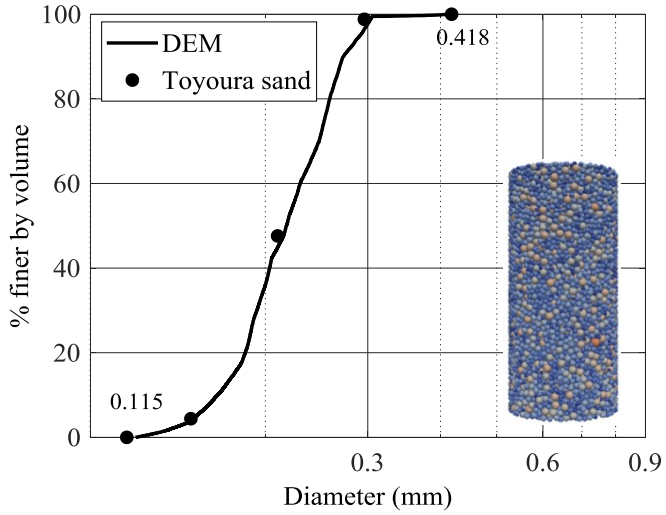

Figure 1 Particle size distribution and configuration of DEM samples

3 Stress–Strain Behavior

Figure 2 shows the stress–strain behavior of the looser sample during cyclic loading. It shows a flow-deformation behavior that is typical for loose sands subject to undrained cyclic loading. The nominal pore water pressure (u) was taken as the difference between the p' value after isotropic compression (p'_0) and the p' value during cyclic loading. As Figure 2a shows, the pore water pressure increases during loading and decreases during unloading in a sinusoidal manner. Initially the pore water pressure accumulates gradually but surges to be close to p'_0 around the 16th loading cycle. This can also be observed in the evolution of stress path in Figure 2b, which shows an abrupt decrease of p' to around 50 kPa. Although p' does not drop to 0, liquefaction is considered to initiate at this instant as the deformation increases in the extension direction in an uncontrollable manner from this instant onwards (Figure 2c and d). The simulation was ceased at the 16th loading cycle as the constant-volume condition was difficult to maintain due to the excessive deformation.

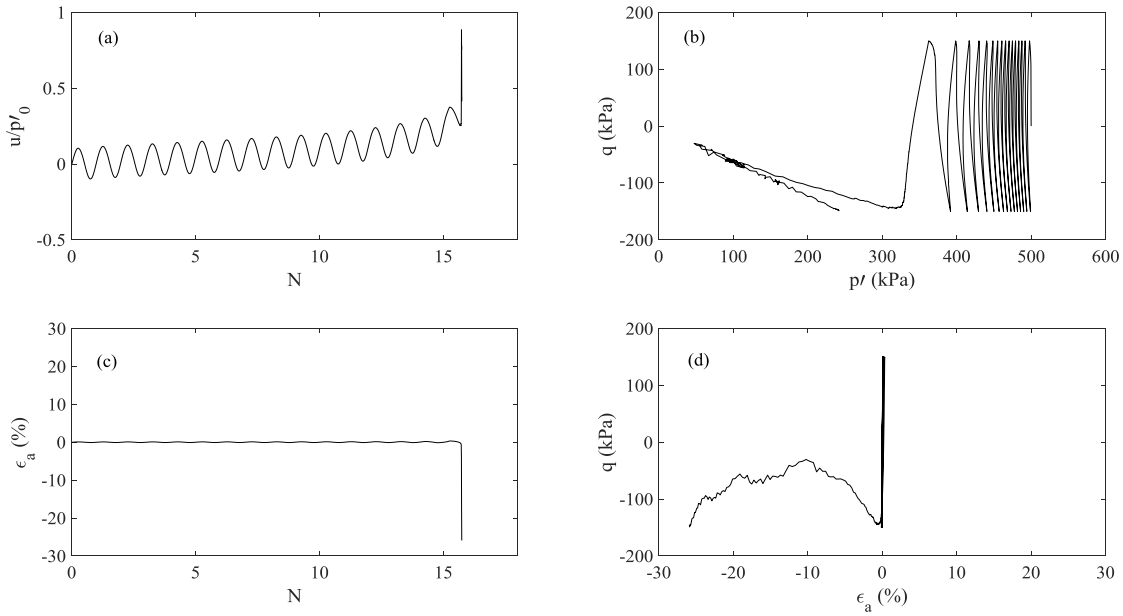

Figure 2 Stress–strain responses of the looser sample showing flow liquefaction behavior: (a) normalized pore water pressure vs number of loading cycles; (b) stress path in q–p' space; (c) axial strain vs number of loading cycles; (d) q vs axial strain

Figure 3 illustrates the stress–strain behavior of the denser sample during cyclic loading. As Figure 3a shows, the pore water pressure increases during loading and decreases during unloading, and is

gradually built up. It momentarily reaches p'_0 at around the 12.5th loading cycle, i.e., initial liquefaction occurs. Once the deviatoric stress becomes non-zero, the pore water pressure drops substantially and the strength and stiffness are recovered due to dilation. This process is repeated in the successive loading cycles. A 'butterfly-shaped' stress path is observed after the 12.5th loading cycle (Figure 3b). The axial strain is small before the 12.5th loading cycle, but becomes notable thereafter and develops in a double-amplitude manner (Figure 3c). Furthermore, most of the deformation is developed at momentary liquefaction instants with $q \approx 0$ (Figure 3d). All of these show the main features of cyclic mobility which is typical for medium dense to dense sands subject to undrained cyclic loading [5].

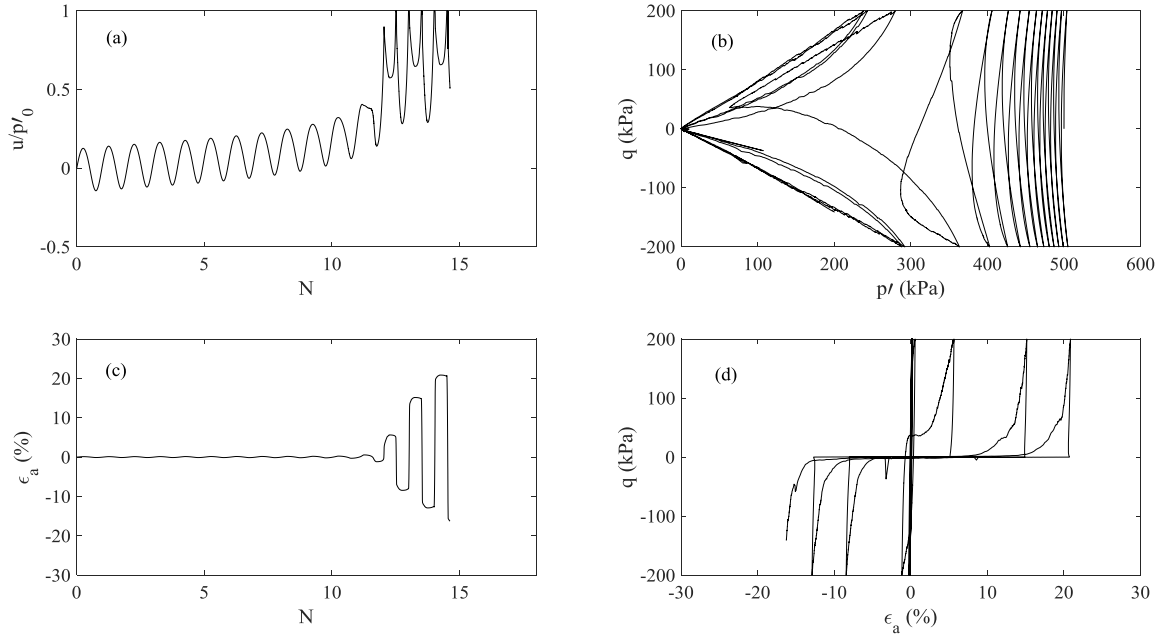

Figure 3 Stress–strain responses of the denser sample showing flow liquefaction behavior: (a) normalized pore water pressure vs number of loading cycles; (b) stress path in q–p' space; (c) axial strain vs number of loading cycles; (d) q vs axial strain

For the looser sample, the effective stress does not drop exactly to zero when flow deformation occurs, whereas the pore water pressure increases to the initial mean effective stress at the onset of liquefaction for the denser sample. For ease of comparison, these two instants are unified as the initiation of failure. Thereby, the number of loading cycles to initiation of failure (N_{IF}) is 16 for the looser sample and 12.5 for the denser sample. Note that the looser sample has a larger N_{IF} than the

denser sample because of a lower q_{cyc}.

4 Mechanical Stability

A granular system, like a sand, is a collection of particles interacting through repulsive and frictional forces at the contacts. If the contacts are viewed as structural members and the particles as nodes, a granular system can essentially be analogous to a composite structure. From a structural mechanics point of view, a composite structure could only maintain its stability (hyperstatic or isostatic) when the number of unknown force components (contact forces) exceeds or equals the number of force and torque balance equations; otherwise, the structure will become hypostatic. Note that when the tangential contact force (f_t) reaches its plastic limit (μf_n, where f_n is the normal contact force), the tangential force will be related to the normal contact force, which reduces the total number of unknown contact forces by $f_s N_c$ (f_s is the fraction of sliding contacts, and N_c is the total number of contacts). Based on these principles and following Shundyak et al. [33], for a 3D system, the minimum number of contacts per particle required to maintain the stability of a granular system is derived:

$$Z_{iso} = 12/(3 - f_s) \quad \text{(Eq. 2)}$$

in which Z_{iso} is the coordination number at the isostatic state. For a system with infinitely large μ ($f_s \approx 0$), Eq. 2 yields Z_{iso} = 4 which is the theoretical minimum isostatic value for a 3D granular system; when either the system is frictionless or all the contacts slide in a frictional system (f_s=1), Z_{iso} = 6 which is the theoretical largest isostatic value for a 3D granular system.

The connectivity of an individual particle can be quantified using the coordination number, which is the average number of particles in contact with an individual particle within a granular system. It also reflects the degree to which an individual particle is kinematically restricted by its neighboring particles. The mechanical coordination number (Z_m) excluding rattlers with fewer than two contacts as defined by Thornton [34] is used herein to describe the average connectivity between particles:

$$Z_m = 2N_c/(N_p - N_p^0 - N_p^1) \quad \text{(Eq. 3)}$$

in which N_p is the total number of particles, N_p^0 and N_p^1 are the numbers of particles with 0 or 1 contact, respectively. A granular system is hyperstatic when Z_m is larger than Z_{iso}, it is isostatic

when Z_m equals to Z_{iso} and becomes hypostatic when Z_m is below Z_{iso}.

Figures 4 and 5 show the evolutions of Z_m, Z_{iso}, and (Z_m - Z_{iso}) during cyclic loading for the looser and denser samples, respectively. For both the looser and the denser samples, Z_m decreases during loading and increases during unloading. The evolution of Z_{iso} is more complex: within a single loading cycle, it increases initially during the first 1/4 loading cycle; it drops abruptly when the loading direction is reversed around the $1/4^{th}$ loading cycle but increases immediately thereafter to the $3/4^{th}$ loading cycle at which it drops again due to reversal of loading direction; it increases immediately again to the end of the loading cycle. For both samples, Z_{iso} is smaller than Z_m before the initiation of failure, which means the number of unknown force components is larger than the number of force and torque equilibrium equations and therefore the system is hyperstatic. An abrupt jump in Z_{iso} is observed at initiation of failure (N/N_{IF} = 1). For the looser sample, after flow occurs, Z_{iso} becomes larger than Z_m, which indicates that the system becomes hypostatic. For the denser sample, Z_m increases but Z_{iso} decreases instantaneously after the initiation of failure, which causes Z_m to exceed Z_{iso} immediately after the momentary liquefaction. Z_m decreases but Z_{iso} increases when approaching each successive liquefaction instant. This procedure is repeated in the process of cyclic mobility. In this sense, cyclic mobility can be viewed as a process of repeating degradation and regaining of the mechanical stability of granular assemblies. As Figure 4(b) and Figure 5(b) show, (Z_m-Z_{iso}) is gradually reduced during cyclic loading and drops abruptly to below zero when flow failure or liquefaction occurs. For the denser sample, during the cyclic mobility period after initial liquefaction (Z_m-Z_{iso}) increases during unloading but decreases during loading. The instant when (Z_m-Z_{iso}) becomes zero exactly coincides with the instant of flow failure or liquefaction.

(Z_m - Z_{iso}) can be used to quantify the distance between the current state and the isostatic state for a granular system and it also quantifies the overall mechanical redundancy of a granular system. The larger this difference is, the more hyperstatic and stable a granular system will be. When this difference approaches zero, the granular system is close to an isostatic state. A granular system will become hypostatic once the difference becomes negative. Figures 4b and 5b indicate that the flow failure or liquefaction process is essentially a process in which a granular system degrades gradually from a hyperstatic state to an isostatic state and then becomes hypostatic at flow failure

or liquefaction instants. The denser sample returns to a hyperstatic state immediately after liquefaction but becomes hypostatic again when approaching successive liquefaction instants in the process of cyclic mobility. In reference to Figures 2 and 3, the deformation is relatively small when the sample is in a hyperstatic state but the sample flows once it becomes hypostatic.

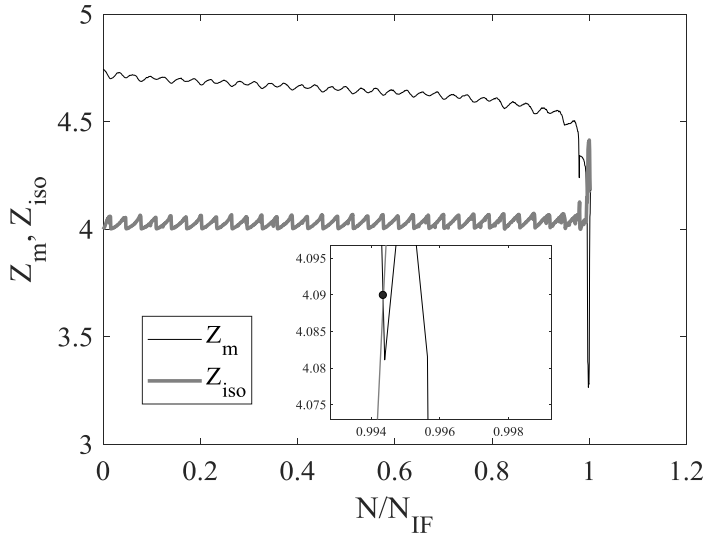

(a)

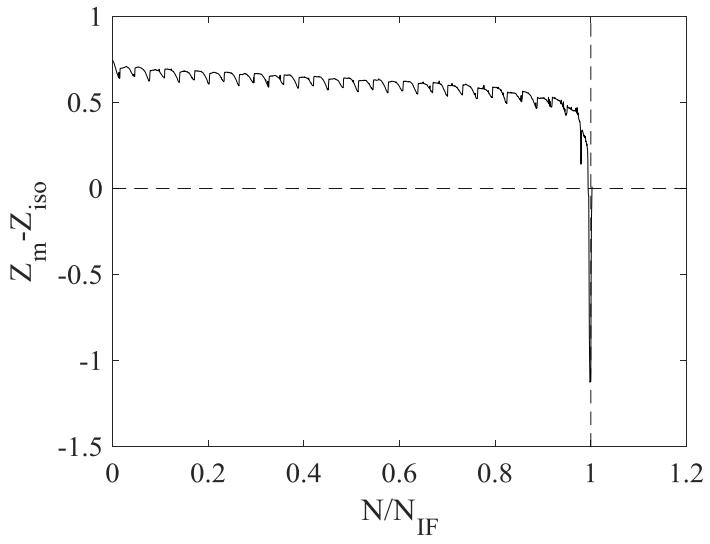

(b)

Figure 4 Evolution of mechanical stability of the looser sample; (a) Z_m and Z_{iso}; (b) Z_m-Z_{iso}

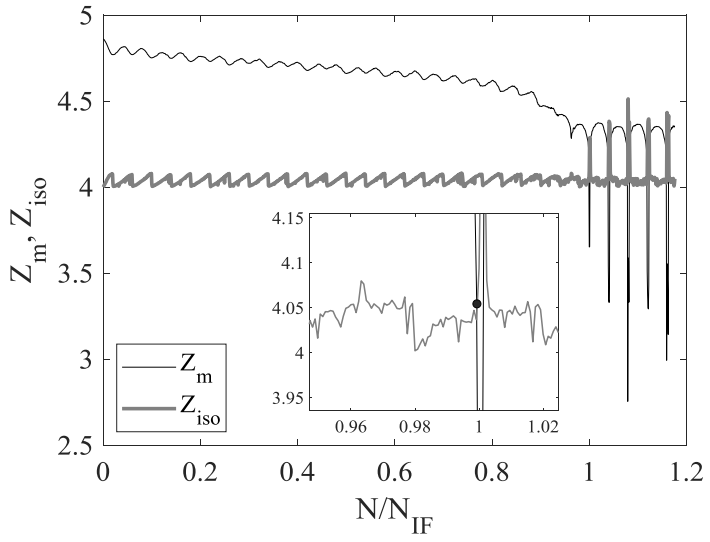

(a)

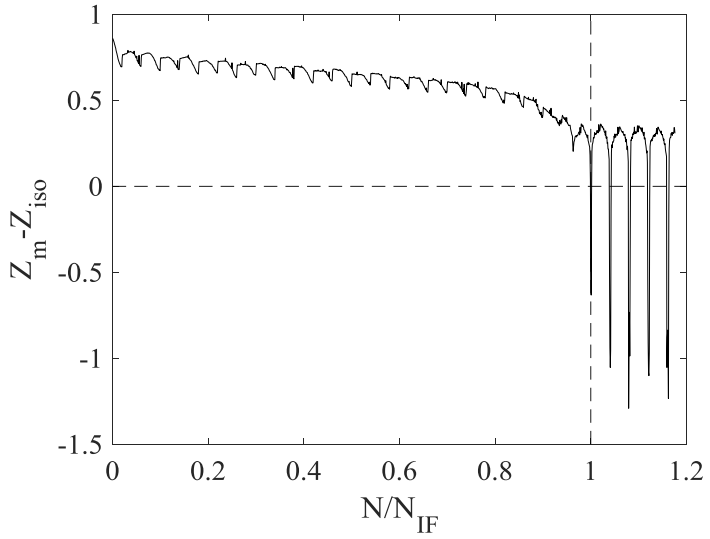

(b)

Figure 5 Evolution of mechanical stability of the denser sample; (a) Z_m and Z_{iso}; (b) Z_m-Z_{iso}

Figures 4 and 5 show the evolution of the overall mechanical stability of the two samples. In fact, the macro stress–strain behavior is also related to the nominal mechanical stability of individual particles which can be quantified by the difference between the number of contacts owned by individual particles (C) and Z_{iso}. To better illustrate how the force transmission networks are degraded and restored during cyclic mobility, the middle slice of X–Z projection of the distributions of (C- Z_{iso}) for the denser sample at characteristic stages of the loading cycle immediately after initial liquefaction (13th loading cycle) are shown in Figure 6. Note that the top rigid plate was fixed and loading–unloading was achieved by moving the bottom rigid plate up

and down. At the beginning of the 13th loading cycle (stage 0), most of the particles do not have enough contacts carried forward from the previous loading cycle to maintain their mechanical stability. Those particles having enough contacting particles to maintain their stability are sparsely distributed within the sample, analogous to isolated islands in a vast ocean. There are almost no stable particles in the top third of the sample. The number of stable particles increases and these gradually become interconnected when the deviatoric strain returns to zero (stage 1). Some stable particles appear close to the top of the sample. When q reaches q_{cyc} (stage 2), a continuous network of stable particles is formed which seems to spread out in both lateral and vertical directions. The elementary particles comprising this continuous network are of high mechanical redundancy. The particles become completely isolated when liquefaction occurs (stage 3) and some stable particles re-appear when the axial strain returns to zero (stage 4). A continuous force transmission network is re-formed when the deviatoric stress reaches q_{cyc} in the extension direction (stage 5) but disintegrates again due to liquefaction (stage 6). Figure 6 shows that a granular system becomes hyperstatic and can sustain external loading without excessive deformation only when mechanically stable particles are integrated throughout the entire sample to form a complex force transmission network. This force transmission network is lost when approaching liquefaction but is regained afterwards due to dilation. This process is repeated during cyclic mobility.

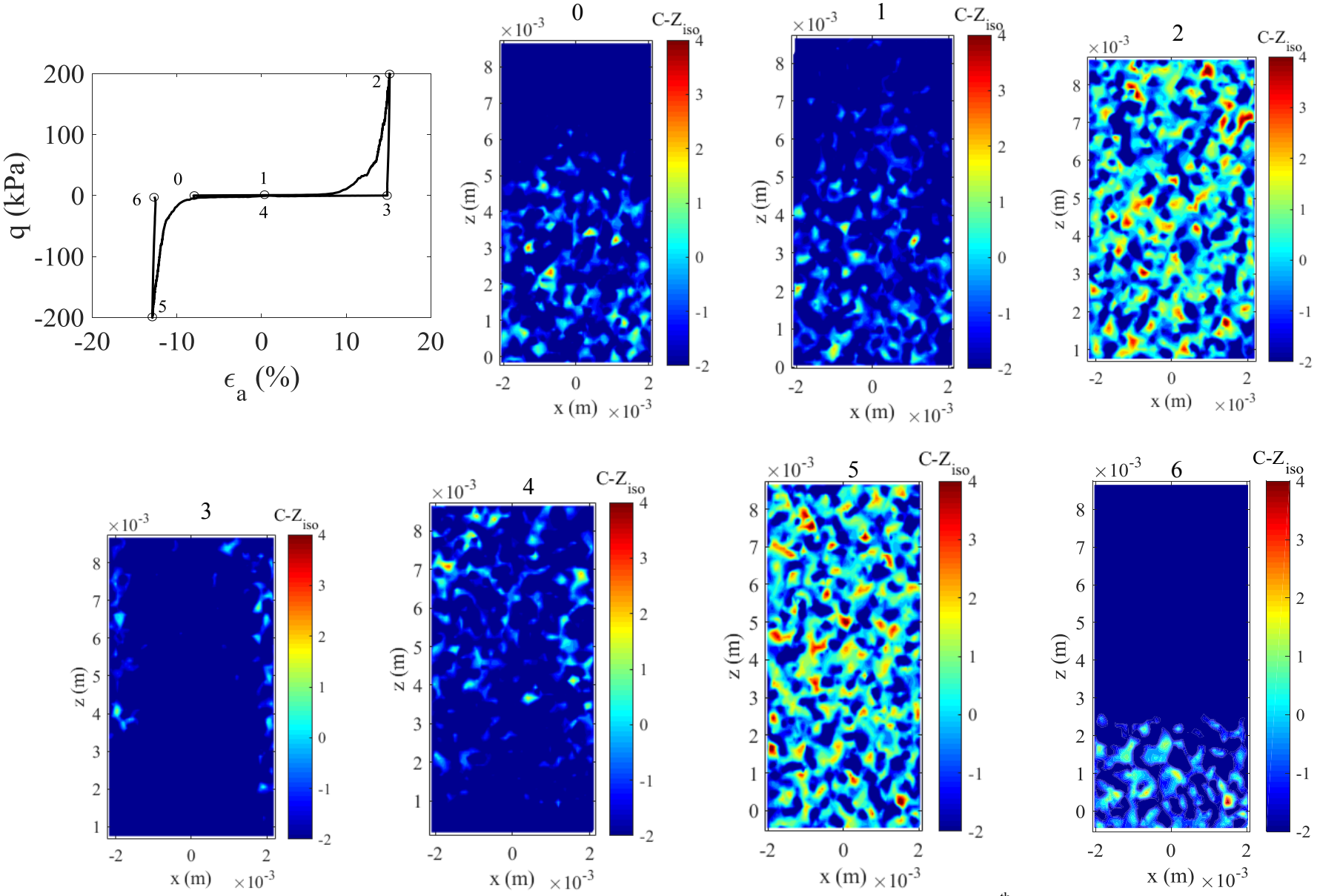

Figure 6 Contours of *X*–*Z* projection of local mechanical stability for the denser sample during the 13th loading cycle (middle slice)

The relationships between p' and (Z_m - Z_{iso}) for the two samples are shown in Figure 7. For both samples, p' decreases as (Z_m - Z_{iso}) decreases and is essentially zero when (Z_m - Z_{iso}) becomes negative, i.e., liquefaction happens when the samples become hypostatic. The liquefaction process is essentially similar to the jammed-to-unjammed transition that has been extensively studied by the physics community [32,35,36]. A jammed system can resist small stresses without deforming irreversibly, whereas unjammed systems flow under any applied stresses [36]. It is widely documented in the physics literature that, subject to isotropic loading, p' on the jammed side ($p' \geq 0$) will scale with (Z_m - Z_{iso}) in a power-law manner when approaching the jamming–unjamming transition point. This is one of the main characteristics of jamming transition [34]. An interesting observation is that the variation of p' with (Z_m - Z_{iso}) before liquefaction can also be represented by the following power-law relationship:

$$p' = m(Z_m - Z_{iso})^{\alpha} + p_a \quad \text{(Eq. 4)}$$

where m, α and p_a are fitting parameters which may depend on many influential factors such as particle shape and PSD as both of them have been shown to significantly affect deformation properties and force transmission [37-40]. Further analysis indicates that if the data in Figure 7 are further divided into different groups according to the magnitude of q, each group of data will still follow Eq. 4, and the coefficient of determination (R^2) will be enhanced from 0.94 when considering them together to over 0.99 when considering them separately. The data are bounded by points at q=0 and q=q_{cyc}. Figure 7 indicates that the fitting parameters m, α and p_a depend on both the deviatoric stress level and the packing density. Furthermore, Figure 7 also shows that variation of p' with (Z_m - Z_{iso}) of the denser sample is more continuous than the looser sample as some notable gaps (marked by dashed cycles in Figure 7a) were observed between successive loading cycles of the looser sample when approaching the initiation of flow. This is associated with the run-out failure characteristics of flow deformation.

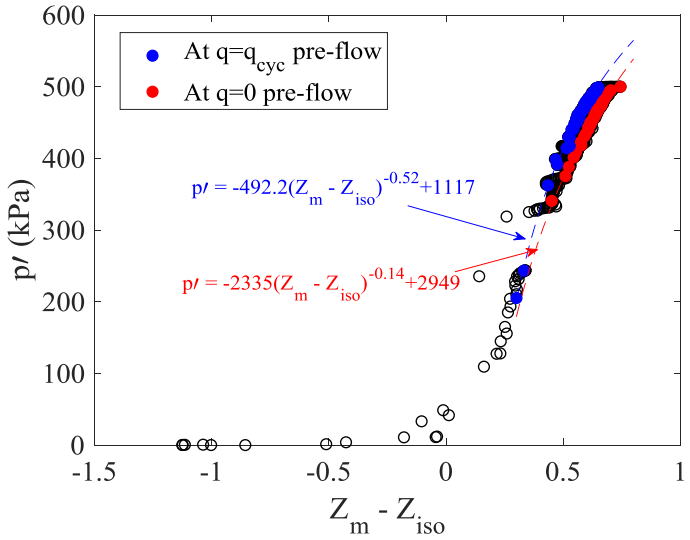

(a)

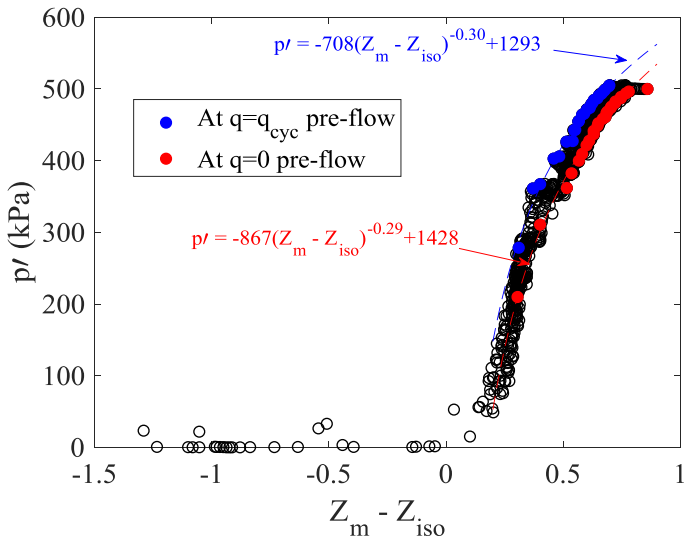

(b)

Figure 7 Relationship between Z_m - Z_{iso}, an index of tendency to flow, and p': (a) looser sample; (b) denser sample (The data points are presented by the hollow circles, while the specific data points at q=q_{cyc} and q=0 pre-flow are marked by blue and red solid circles, respectively.)

5 Reversibility Analysis

The bearing capacity of a granular system and its deformation characteristics also depend on the ability of its force transmission network to sustain external load and resist deformation in loading–unloading cycles. It is noteworthy that the micro-structure of a frictional granular system cannot fully recover due to the inevitable energy dissipation induced by particle sliding, collision and

rearrangement. Therefore, the reversibility herein reflects the extent to which the force transmission network can recover in loading–unloading cycles by measuring the variations of mean squared displacement (MSD), fraction of broken contacts (B_L) and size of the largest force transmission network (S_L) following Slotterback et al. [41].

5.1 Mean squared displacement (MSD)

The MSD quantifies the average absolute displacement of particles within a granular system subject to external loading and is defined as:

$$MSD = (\sum_{i=1}^{N_p}((\Delta x_i)^2 + (\Delta y_i)^2 + (\Delta z_i)^2))/N_p \quad \text{(Eq. 5)}$$

in which Δx_i, Δy_i and Δz_i are displacement increments of particle i with respect to the initial state prior to cyclic loading. The scaling law of MSD with time reflects the deformation capacity as well as the deformation mode of a granular system in the presence of external shearing: if MSD scales linearly with time, the system is normal diffusive and the particle motion follows a Brownian mode; if MSD scales with time in a power-law manner with a power smaller than 1, the system is sub-diffusive; if MSD scales with time in a power-law manner with a power larger than 1, the system is super-diffusive [42]. The second and third cases are called anomalous diffusion. Figure 8 shows the variation of MSD at the end of each loading cycle. For both samples, MSD varies almost linearly with the number of loading cycles (N) before liquefaction on this double-logarithmic figure. The slope of this relationship approximates 1, indicating that the system is normal diffusive [43]. In such a case, the residual particle motion induced by loading–unloading is approximately equal between different loading cycles. For the denser sample, the slope starts to increase at around the 12th loading cycle: one cycle before the loading cycle in which liquefaction is initiated. For the looser sample, a dramatic change in the slope is observed when flow occurs. The increase of slope in Figure 8 indicates that the system is transitioning from normal diffusion (slope =1 in the double-lognormal space) towards super diffusion (slope > 1 in the double-lognormal space) when approaching liquefaction. The particles move significantly larger distances and deviate more from their original positions to accommodate the same external loading after liquefaction has occurred; thus, the particle motion is no longer Brownian and the two samples become increasingly irreversible post-liquefaction.

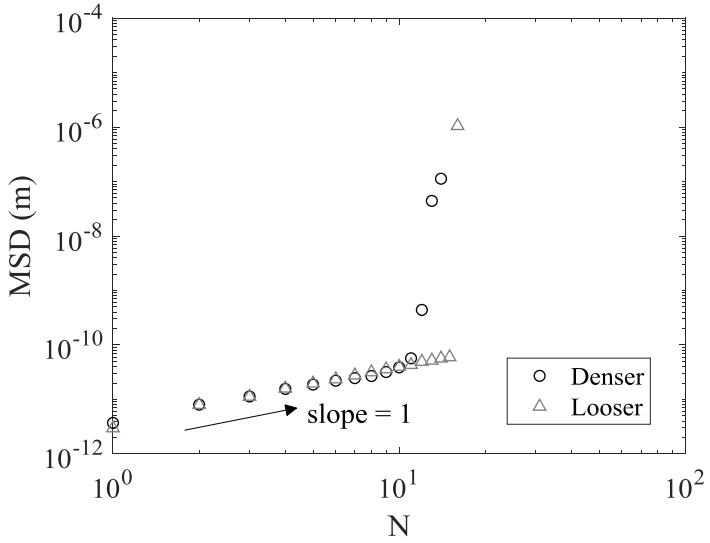

Figure 8 Variation of mean square displacement (MSD) at the end of loading cycles relative to initial position with N

5.2 Fraction of broken contacts (f_b)

As noted by Hanley et al. [44], the contact network of a granular system is not constant but evolves dynamically during loading. Some particles which were initially in contact separate and some new contacts are formed subject to external loading. This variation of the local topology surrounding an individual particle reflects variations in the force transmission network and is closely related to the external loading conditions [44]. The fraction of broken contacts (f_b) is defined as the ratio of the number of broken contacts to the total number of contacts at the reference frame. f_b is used herein to quantify the average change of neighborhood conditions of individual particles within the two samples relative to a reference frame. A more resilient force transmission network is expected to experience fewer contact breakage events subject to the same loading conditions than a less resilient network.

Figure 9a shows the evolution of f_b throughout the entire loading process, relative to the initial isotropic state (termed $f_{b,0}$). We firstly identify the contacting particles at the start of cyclic loading. Then we calculate the fraction of contacting pairs that separate in the subsequent loading process by comparing the current contact list to the original one before shearing. For both the looser and the denser samples, $f_{b,0}$ increases during loading (increasing q) but decreases during unloading (decreasing q). For the looser sample, an abrupt change in $f_{b,0}$ is observed when approaching flow failure whereas, for the denser sample, $f_{b,0}$ increases more gradually approaching liquefaction. $f_{b,0}$

is higher for the denser sample than for the looser one, which may be attributed to the larger critical stress ratio (CSR) applied. The $f_{b,0}$ values post-liquefaction remain greater than 0.6 and exceed 0.8 at liquefaction instants, which indicates that almost all of the contacts re-formed post-liquefaction are short-lived. As Figure 9b shows, $f_{b,0}$ at the end of a loading cycle increases almost linearly as cyclic loading proceeds, indicating that the reversibility of the force transmission network decreases continuously in the process of cyclic loading.

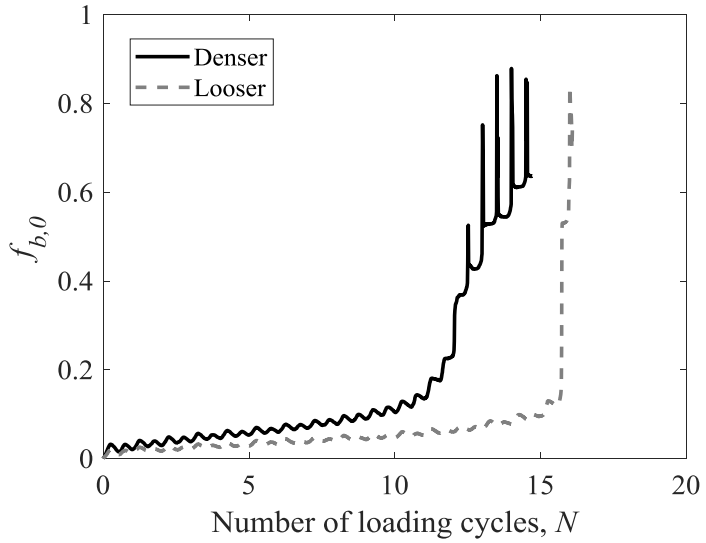

(a)

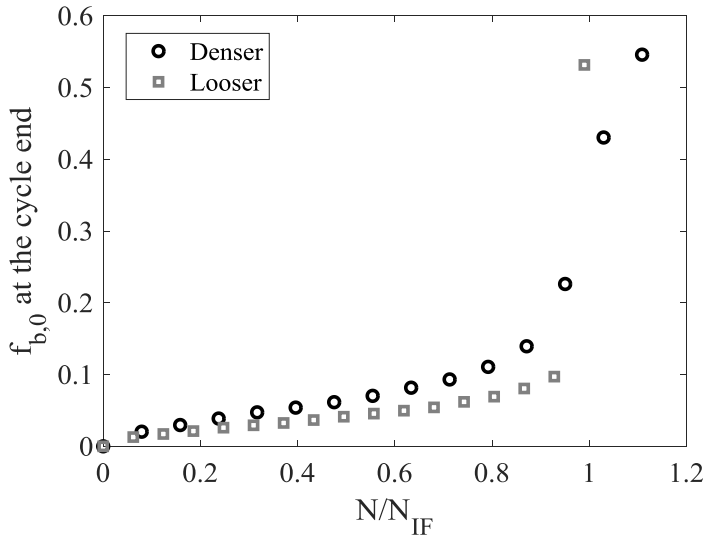

(b)

Figure 9 Evolution of fraction of broken contacts relative to the initial isotropic state versus the fraction of cycle N: (a) throughout the simulations; (b) at the end of loading cycles

Consider now a change of the reference frame from the initial state to the start of each loading

cycle. Figure 10 plots f_b for each cycle relative to the start of cycle N (termed $f_{b,N}$). The color indicates the number of loading cycles. Overall, $f_{b,N}$ increases with increasing N. $f_{b,N}$ is very small for the first few cycles. For the looser sample, before the 16th loading cycle, $f_{b,N}$ increases during loading but decreases during unloading. An abrupt increase in $f_{b,N}$ occurs at $N \approx 15.7$, reaching about 0.53 around $N = 15.75$. Thereafter, $f_{b,N}$ remains approximately constant until $N \approx 15.9$, before increasing to 0.84 at the end of the 16th loading cycle. For the denser sample, obvious changes in $f_{b,N}$ between successive loading cycles are observed after the 11th loading cycle. In particular, the variation of $f_{b,N}$ no longer follows a trend of increasing for increasing q and decreasing for decreasing q. It only changes at instants close to the start, the middle and the end states of a loading cycle and remains approximately constant between these states. This striking feature indicates that the contact network post-liquefaction may have reached a threshold state in which the force transmission network contains just enough contacts to sustain the external loading and the structure is completely irreversible.

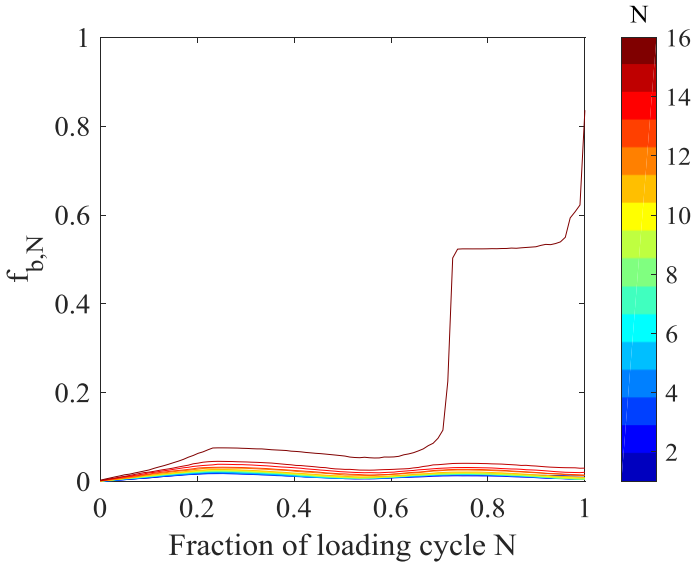

(a)

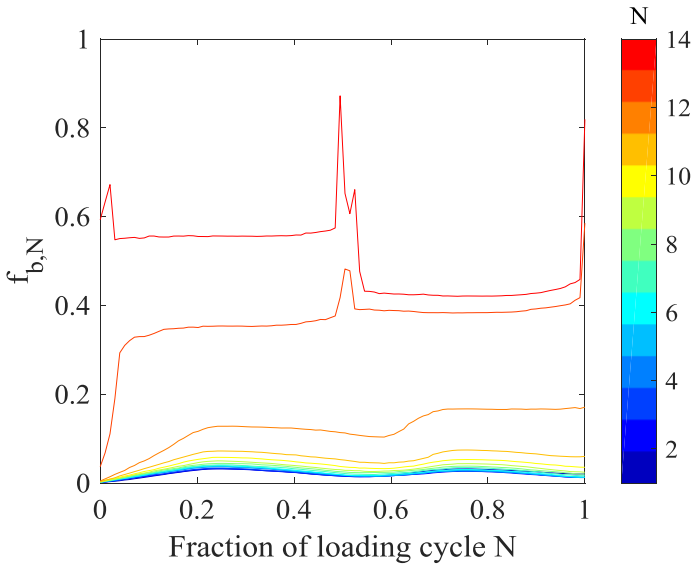

(b)

Figure 10 Evolution of fraction of broken contacts relative to the start of cycle N versus the fraction of cycle N: (a) looser sample; (b) denser sample

Figure 11 plots $f_{b,N}$ at the end of each loading cycle against the number of loading cycles normalized by the number of cycles to initial failure (N_{IF}). For both samples, this relationship can be divided into three phases:

a) Phase I: increasing reversibility. $f_{b,N}$ decreases between the 1st and 2nd loading cycles. This is understandable as more drastic particle rearrangement is expected in the 1st loading cycle in which the force transmission network changes from isotropic to anisotropic.

b) Phase II: $f_{b,N}$ remains approximately constant between the 2nd and 5th loading cycles for the denser sample and between the 2nd and 9th loading cycles for the looser sample. These plateaus indicate that the two samples are in reversible-to-irreversible transition states.

c) Phase III: increasing irreversibility. At this stage, $f_{b,N}$ increases continuously and contact conditions vary severely and frequently.

The evolution of f_b is closely related to that of MSD. Referring to Figure 8, the MSD is tiny and remains almost constant before the 7th or the 15th loading cycles (denser and looser samples, respectively). In this picture, a small fraction of broken contacts leads to small localized failures; however, these contacts are mostly re-formed upon reversal. Most of the particles return to their original positions, leading to a small MSD. However, once the fraction of broken contacts becomes sufficiently large, these regions of local failure become interconnected and propagate

throughout the entire sample (see Figure 6). Upon stress reversal, the separated contacts can no longer be fully recovered, and after one cycle, the particles end up with different neighbors and deviate from their positions at the start of that loading cycle, leading to a large MSD. This is the origin of flow deformation for the looser sample and development of significant double-amplitude strains for the denser sample.

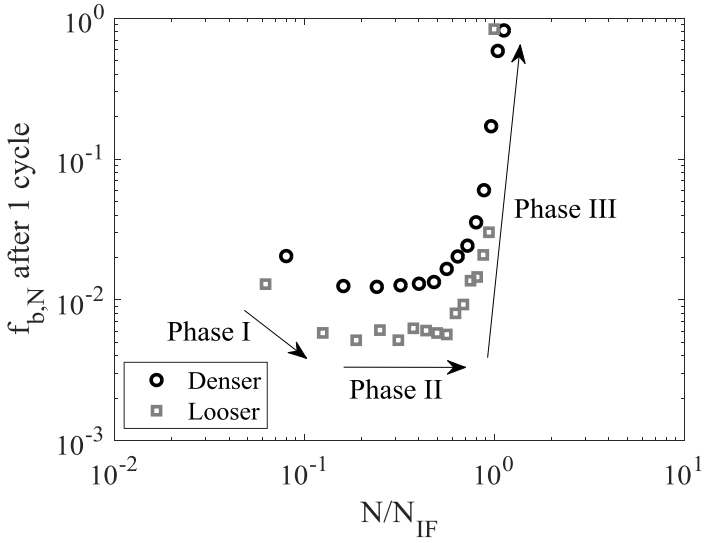

Figure 11 Relationships between $f_{b,N}$ at the end of a loading cycle with the normalized number of loading cycles

5.3 Size of the largest force transmission network (S_L)

The external loads experienced by a granular system are transmitted through interparticle contacts. The particles of a granular system are not all connected together. There exists a certain number of clusters composed of different numbers of contacting particles within a granular system. Identification of a cluster started from searching the neighbor list of a single particle. The search procedure proceeded recursively for all the identified particles according to the sequence of neighbors given in the contact list until all of the particles comprising the cluster had been identified. Other clusters could be identified following the same procedure by starting from particles not already included in a cluster. The cluster having the most particles is taken as the largest force transmission network. Since gravity is absent, clusters are isolated from each other. Figure 12 shows the evolution of the number of clusters of contacting particles (N_{cl}) normalized by the total number of particles (N_p) during cyclic loading. The larger N_{cl}/N_p is, the smaller the

average size of clusters will be. For both samples, N_{cl}/N_p is small before initial failure, which indicates that the contact network has a high degree of percolation. For the looser sample, N_{cl}/N_p jumps momentarily to over 0.6 at liquefaction instants, indicating that the clusters are distributed and particles are isolated (see Figure 6). For the denser sample, N_{cl}/N_p decreases after initial liquefaction but increases again when approaching the successive liquefaction instants. Before the onset of liquefaction, apart from the largest cluster which contains the majority of particles, the remaining clusters are mostly rattlers with one or two neighboring particles. At liquefaction instants, almost all the particles are isolated. The number of particles that a cluster contains becomes more divergent immediately post-liquefaction. These small clusters aggregate rapidly into the largest force transmission network at the initial stage of the recovering process of strength and stiffness but disintegrate again when approaching liquefaction.

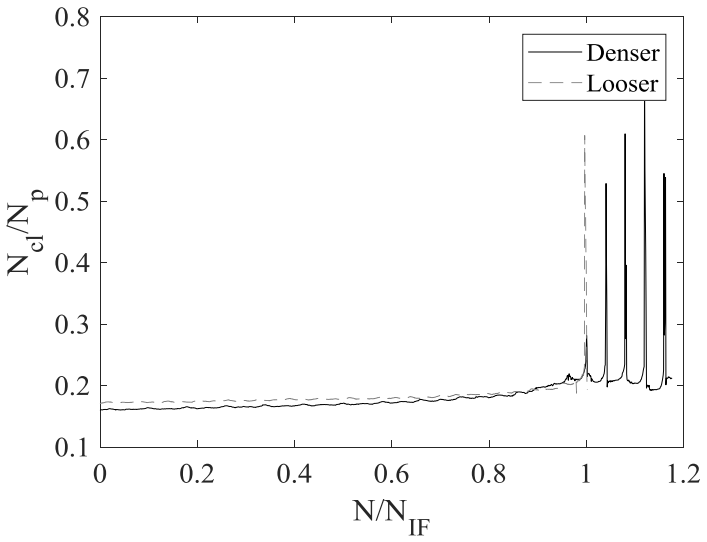

Figure 12 Evolution of the number of clusters (N_{cl}) normalized by the number of particles (N_p) against the normalized number of loading cycles

The more particles contributing to the largest contact network, the more stable and resilient the sample will be. Figure 13 shows the evolution of the size of the largest force transmission network (S_L) which is defined as the ratio of the number of particles within the largest force transmission network to the total number of particles. S_L is initially 0.84 or 0.83 for the denser and looser samples, respectively. It decreases gradually during loading and increases gradually during unloading until it is reduced to 0.74, after which S_L drops abruptly to be less than 0.4. The sudden drop of S_L coincides with the occurrence of flow deformation or liquefaction, which indicates that

there may exist a critical size of the major force transmission network, below which the force transmission network becomes hypostatic and is unable to sustain external loads. For the denser sample, after momentary liquefaction, small clusters coalesce again to form a large contact network with an S_L value larger than 0.76 and the sample regains its strength and stiffness. Figure 13b plots S_L against q. For both samples, S_L degrades gradually as cyclic loading proceeds. Both samples can only sustain a small q when S_L is below 0.76 and S_L decreases significantly. This is associated with the flow deformation of the looser sample and the development of obvious double-amplitude axial strain of the denser sample. S_L of the denser sample increases immediately post-liquefaction and the sample is able to sustain q again when S_L becomes larger than 0.76.

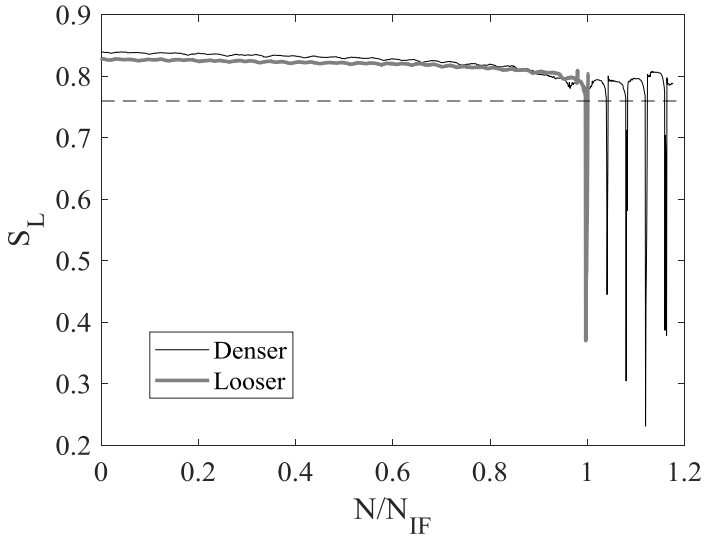

(a)

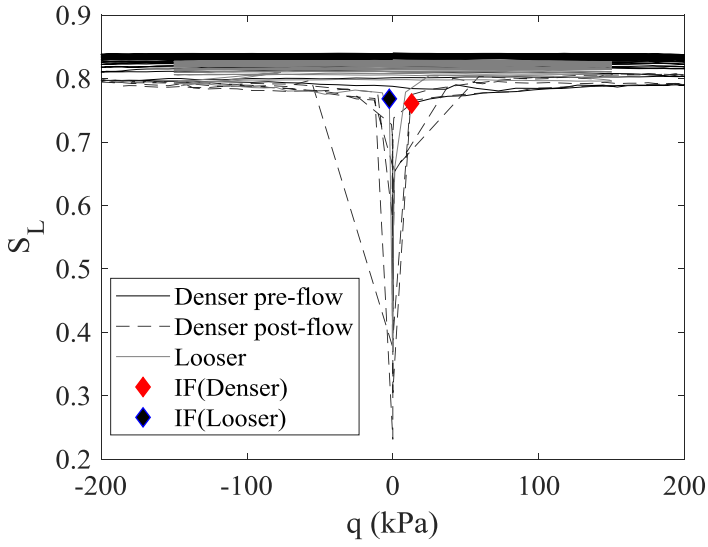

(b)

Figure 13 Evolution of the size of the largest force transmission network, S_L, with: (a) N/N_{IF} (b) q

S_L is also closely related to p'. As Figure 14 shows, at the instants of both the most isotropic (q=0) and the most anisotropic loading states (q=q_{cyc}), S_L decays perfectly linearly with p' before liquefaction with R^2 values being over 0.99. The fitting parameters of the linear correlations between S_L and p' seem to be slightly dependent on the magnitude of q and packing density. S_L drops abruptly when liquefaction occurs (p'=0). Extrapolating the fitting equations given in Figure 14 to p'=0 indicates that the critical value of S_L below which liquefaction occurs is between 0.717 and 0.744.

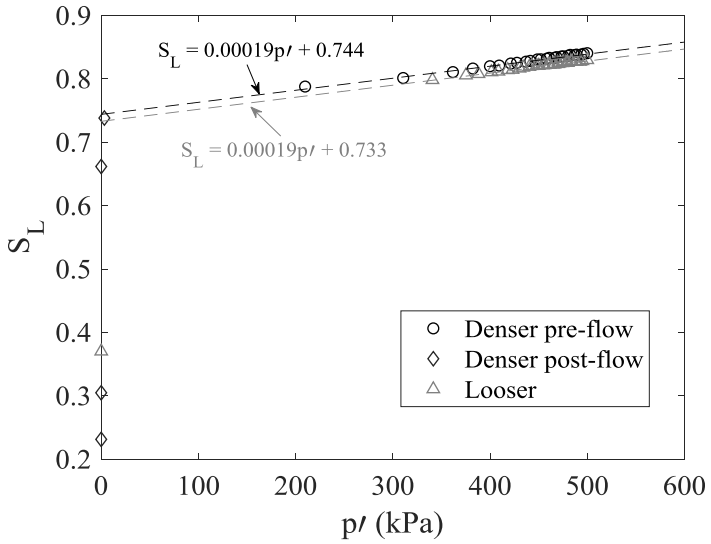

(a)

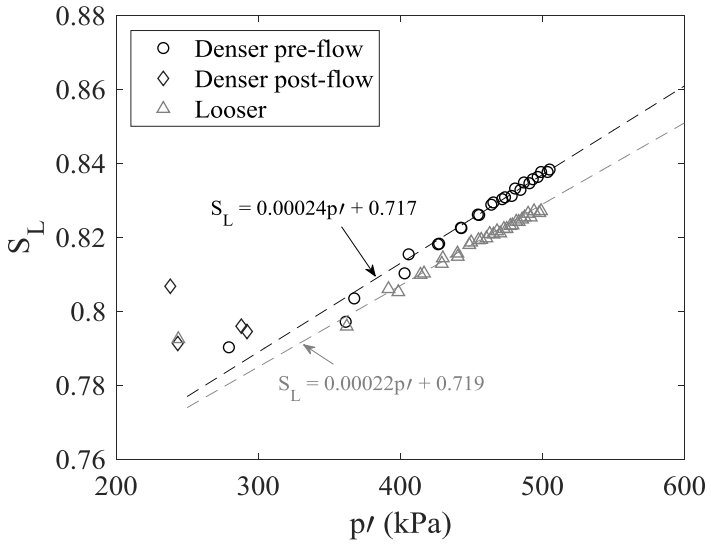

(b)

Figure 14 Relationships between the size of the largest force transmission network, S_L, and mean effective stress, p' at: (a) q=0 (b) q=q_{cyc}

6 Conclusion

DEM simulations were performed to investigate the structural degradation and its correlations with the macro stress–strain behavior of sands subject to undrained cyclic loading. Both flow-type failure for loose sand and cyclic mobility for medium dense to dense sand subject to undrained cyclic loading were captured. The variation of mechanical stability of the DEM assemblies during cyclic loading was evaluated by comparing the difference between the mechanical coordination number (Z_m) and the isostatic coordination number (Z_{iso}). The change of reversibility of the DEM samples during cyclic loading were explored by measuring the mean squared displacement (MSD), fraction of broken contacts (f_b) and size of the largest force transmission network (S_L). The following observations are made:

(a) The liquefaction process can be described as a process during which the mechanical state degrades from hyperstatic to isostatic and eventually becomes hypostatic after initial liquefaction. The difference between the mechanical coordination number and the isostatic coordination number before the occurrence of liquefaction is related to the mean effective stress in a power-law manner with a deviation term.

(b) An effective load-bearing contact network is formed only when enough mechanically stable particles are interconnected. The stability of individual particles decreases and the clusters composed of mechanically stable particles gradually disintegrate during cyclic loading. Particles become more isolated and the mechanical stability becomes increasingly localized upon liquefaction.

(c) The reversibility of the force transmission network decreases during cyclic loading, which is characterized by increasing MSD, fraction of broken contacts and decreasing size of the largest force transmission network. Overall, the reversibility before liquefaction decreases with increasing absolute value of q. The reversibility drops abruptly upon liquefaction. It recovers immediately after momentary liquefaction but drops again at successive liquefaction instants in the process of cyclic mobility.

(d) Prior to the initiation of flow failure or liquefaction, most of the interparticle contacts that are

lost during a cycle are re-formed shortly afterwards when the loading direction is reversed, and particles only deviate slightly from their initial positions after a complete loading cycle. Therefore, the deformation of sands is small prior to initial liquefaction. However, when approaching liquefaction, many broken contacts do not re-form in the subsequent loading. Consequently, the particles experience large displacements and can rarely return to their original positions after a complete loading cycle. This is the fundamental mechanism underlying the flow deformation of the loose sample and the progressive development of double-amplitude strain during cyclic mobility of medium dense and dense sands.

(e) There exists a critical size of the largest force transmission network. When S_L is larger than this critical value, the sample is stable and can sustain some deviatoric load. However, when S_L falls below this critical value, the sample becomes hypostatic, and can no longer sustain deviatoric loading, and liquefaction occurs.

These observations reveal that the degradation of reversibility and stability of the force transmission network are closely related to the changes of strength and deformation of sand both before and after liquefaction. This specific feature and the correlation between S_L and mean effective stress established in the current study, apart from the anisotropy indices, may be useful for advanced constitutive modeling of sand considering micro-structure evolution. Finally, it should be noted that the current study only qualitatively reflects the fundamental mechanism underlying soil liquefaction due to the use of spherical particles. For quantitative study, one should build up models considering the irregularity of soil grains.

Acknowledgement

This research is funded by the National Natural Science Foundation of China (No. 51509186 & 41877227) and the National Key Research and Development Program of China (2017YFC0806004).

References

[1] Castro G. Liquefaction and cyclic mobility of saturated sands. Journal of the Geotechnical Engineering Division 1975; 101(6): 551-569

[2] Seed HB, Lee KL. Liquefaction of saturated sands during cyclic loading. Journal of the Soil Mechanics and Foundations Division 1966; 92(6): 105–134

[3] Hyodo M, Tanimizu H, Yasufuku N, Murata H. Undrained cyclic and monotonic triaxial behaviour of saturated loose sand. Soils and Foundations 1994; 34(1): 19-32

[4] Vaid, YP, Sivathayalan S. Static and cyclic liquefaction potential of Fraser Delta sand in simple shear and triaxial tests. Canadian Geotechnical Journal 1996; 33: 281-289

[5] Yang J, Sze HY. Cyclic behaviour and resistance of saturated sand under non-symmetrical loading conditions. Géotechnique 2011; 61(1): 59-73

[6] Yang J, Sze HY. Cyclic strength of sand under sustained shear stress. Journal of Geotechnical and Geoenvironmental Engineering 2011; 137(12): 1275-1285

[7] Sze HY, Yang J. Failure modes of sand in undrained cyclic loading: Impact of sample preparation. Journal of Geotechnical and Geoenvironmental Engineering 2014; 140(1): 152-169

[8] Oka F, Yashima A, Tateishi A, Taguchi Y, Yamashita S. A cyclic elasto-plastic constitutive model for sand considering a plastic-strain dependence of the shear modulus. Géotechnique 1999; 49(5): 661-680

[9] Li XS. A sand model with state-dependent dilatancy. Géotechnique 2002; 52(3): 173-186

[10] Elgamal A, Yang ZH, Parra E, Ragheb A. Modeling of cyclic mobility in saturated cohesionless soils. International Journal of Plasticity 2003; 19: 883-905

[11] Yin ZY, Chang CS, Hicher PY. Micromechanical modelling for effect of inherent anisotropy on cyclic behavior of sand. International Journal of Solids and Structures 2010; 47: 1933–1951

[12] Gao ZW, Zhao JD. Constitutive modeling of anisotropic sand behavior in monotonic and cyclic loading. Journal of Engineering Mechanics 2015; 141(8): 04015017

[13] Wei JT, Huang DR, Wang G. Microscale descriptors for particle-void distribution and jamming transition in pre- and post-liquefaction of granular soils. Journal of Engineering Mechanics 2018; 144(8): 04018067

[14] Cundall PA, Strack ODL. A discrete numerical model for granular assemblies. *Géotechnique* 1979; 29(1): 47–65

[15] O'Donovan J, O'Sullivan C, Marketos G. Two-dimensional discrete element modelling of bender element tests on an idealised granular material. Granular Matter 2012; 14(6): 733-747

[16] Gu XQ, Yang J, Huang MS. DEM simulations of the small strain stiffness of granular soils: effect of stress ratio. Granular Matter 2013; 15(3): 287-298

[17] Ning Z, Khoubani A, Evans TM. Shear wave propagation in granular assemblies. Computers and Geotechnics 2015; 69: 615-626

[18] Guo N, Zhao JD. The signature of shear-induced anisotropy in granular media. Computers and Geotechnics 2013; 47: 1-15

[19] Huang X, Hanley KJ, O'Sullivan C, Kwok CY. Discrete-element method analysis of the state

parameter. Géotechnique 2014; 64: 954-965
[20] Ng, T-T, Dobry, R. Numerical simulations of monotonic and cyclic loading of granular soil. Journal of Geotechnical Engineering 1994; 120(2): 388–403.
[21] Sitharam, TG. Discrete element modelling of cyclic behaviour of granular materials. Geotechnical and Geological Engineering 2009; 21(4): 297–329.
[22] Kuhn, MR, Renken HE, Mixsell AD, Kramer SL. Investigation of cyclic liquefaction with discrete element simulations. Journal of Geotechnical and Geoenvironmental Engineering 2014; 140(12): 1-13
[23] Xu XM, Ling DS, Cheng YP, Chen YM. Correlation between liquefaction resistance and shear wave velocity of granular soils: a micromechanical perspective. Géotechnique 2015; 65(5): 337-348
[24] Huang X, Kwok CY, Hanley KJ, Zhang, ZX. DEM analysis of the onset of flow deformation of sands: linking monotonic and cyclic undrained behaviours. Acta Geotechnica 2018; 13: 1061–1074
[25] Wang G, Wei JT. Microstructure evolution of granular soils in cyclic mobility and post-liquefaction process. Granular Matter 2016; 18: 51
[26] Wang R., Fu PC, Zhang JM & Dafalias YF. DEM study of fabric features governing undrained post-liquefaction shear deformation of sand. Acta Geotechnica 2016; 11(6): 1321-1337
[27] Tordesillas A, Zhang J, Behringer R. Buckling force chains in dense granular assemblies: physical and numerical experiments. Geomechanics and Geoengineering: An International Journal 2009; 4(1): 3–16
[28] Huang X, O'Sullivan C, Hanley KJ, Kwok C-Y. Partition of the contact force network obtained in discrete element simulations of element tests. Computational Particle Mechanics 2017; 4(2): 145–152
[29] Itasca Consulting Group. Particle Flow Code in Three Dimensions: User's Manual, Version 4.0. Minneapolis, USA 2007
[30] Huang X, Hanley KJ, O'Sullivan C, Kwok C-Y. Exploring the influence of interparticle friction on critical state behaviour using DEM. International Journal for Numerical and Analytical Methods in Geomechanics 2014; 38(12): 1276-1297.
[31] Ishihara K. Liquefaction and flow failure during earthquakes. Géotechnique 1993; 43(3): 351-451
[32] Wei X, Yang J. Cyclic behavior and liquefaction resistance of silty sands with presence of initial static shear stress. Soil Dynamics and Earthquake Engineering 2019; 122: 274-289
[33] Shundyak K., van Hecke M, van Saarloos W. Force mobilization and generalized isostaticity in jammed packings of frictional grains. Physical Review E 2007; 75: 010301(R)
[34] Thornton C. Numerical simulations of deviatoric shear deformation of granular media. Géotechnique 2000; 50(1): 43–53
[35] Somfai E, Van Hecke M, Ellenbroek WG, Shundyak K, van Saarloos W. Critical and noncritical jamming of frictional grains. Physical Review E 2007; 75(1): 020301
[36] Bi D, Zhang J, Chakraborty B, Behringer RP. Jamming by shear. Nature 2011; 480(7377): 355-358
[37] Cho G-C, Dodds J, Santamarina JC. Particle shape effects on packing density, stiffness, and strength: natural and crushed sands. Journal of Geotechnical and Geoenvironmental

Engineering 2006; 132(5): 591-602
[38] Yan WM, Dong JJ. Effect of particle grading on the response of an idealized granular assemblage. International Journal of Geomechanics 2007; 11(4): 276-285
[39] Maeda K, Sakai H, Kondo A, Yamaguchi T, Fukuma M, Nukudani E. Stress-chain based micromechanics of sand with grain shape effect. Granular Matter 2010; 12(5): 499-505.
[40] Minh NH, Cheng YP, Thornton C. Strong force networks in granular mixtures. Granular Matter 2014; 16(1): 69-78
[41] Slotterback S, Mailman M, Ronaszegi K, van Hecke M, Girvan M, Losert W. Onset of irreversibility in cyclic shear of granular packings. Physical Review E 2012; 85: 021309.
[42] Sharifi-Viand A, Mahjani MG, Jafarian M. Investigation of anomalous diffusion and multifractal dimensions in polypyrrole film. Journal of Electroanalytical Chemistry 2012; 671: 51-57
[43] Kou B, Cao Y, Li J, Xia C, Li Z, Dong H, Zhang A, Zhang J, Kob W, Wang YJ. Granular materials flow like complex fluids. Nature 2017; 551(7680): 360-363
[44] Hanley KJ, Huang X, O'Sullivan C, Kwok CY. Temporal variation of contact networks in granular materials. Granular Matter 2014; 16: 41-54